

Fast salt boundary interpretation with optimal path picking

Xinming Wu¹, Sergey Fomel¹, and Michael Hudec¹

ABSTRACT

Salt boundary interpretation is a crucial step for velocity-model building in seismic migration, but it remains a highly labor-intensive task for manual interpretation and a big challenge for automatic methods. We have developed a semiautomatic method to efficiently and accurately extract 2D and 3D complicated salt boundaries from a seismic attribute image that highlights salt boundaries. In 2D salt boundary extraction, we first pick a few points to interpolate an initial curve that is close to the true salt boundary. These points are picked near the salt boundary but are not required to be exactly on the boundary, which makes human interactions convenient and efficient. We then resample the salt boundary attribute image in a band area centered at the initial curve to obtain a new image in which the

true salt boundary is an open curve extending laterally. We then extract the salt boundary in the new image using an optimal-path picking algorithm, which is robust enough to track a stable salt boundary from highly discontinuous attribute values by solving a global maximization problem. We finally map the picked path back to the original image to obtain a final salt boundary. In 3D salt boundary extraction, we apply the 2D method to recursively pick 2D salt boundaries in a sequence of inline or crossline slices and then use these 2D boundaries to fit an implicit (level-set) surface of the 3D salt boundary. In our recursive picking, human interactions are greatly reduced by using a salt boundary picked in the previous slice as an initial curve for picking in a followed slice. The effectiveness of our method is confirmed with 2D and 3D real seismic images.

INTRODUCTION

Salt boundary interpretation is important for studying salt tectonics (Hudec et al., 2011; Jackson and Hudec, 2016) and for velocity-model building in seismic migration (Wang et al., 2008; Leveille et al., 2011). Interpreting salt boundaries often involves computing a salt attribute image and picking salt boundaries from the attribute image. Such an attribute image can be a seismic envelope image, in which salt boundaries can be recognized as reflections with relatively high envelope values. Other seismic attributes including discontinuities (Jing et al., 2007; Aqrabi et al., 2011; Asjad and Mohamed, 2015), textures (Berthelot et al., 2013; Hegazy and Al-Regib, 2014; Wang et al., 2015), reflection dip or normal vector fields (Halpert and Clapp, 2008; Haukås et al., 2013), and salt likelihoods (Wu, 2016) are also used to highlight salt boundaries. Different from seismic envelopes, all these attributes are based on the observations that the seismic reflections, inside and outside a salt boundary, are often differently oriented across the salt boundary.

After computing a salt attribute image, the next step is to extract salt boundaries, which is also discussed by previous authors. Some authors (Lomask et al., 2007; Dahlke et al., 2016; Ramirez et al., 2016) consider salt boundary extraction as a global image segmentation problem. Zhang and Halpert (2012) and Haukås et al. (2013) use active-contour-based methods to gradually deform an initially defined shape to fit a salt boundary. Some other authors (Halpert et al., 2014; Amin and Deriche, 2015; Di and AlRegib, 2017; Di et al., 2017) extract salt boundaries by combining multiple types of attributes. Wu (2016) simultaneously extract multiple salt boundaries by solving a Poisson's equation constructed from a previously computed salt likelihood image.

Although automatic methods have been proposed for computing salt attributes and extracting salt boundaries, salt boundary interpretation today remains a human-intensive and time-consuming task. In practice, a salt boundary can be extremely complicated by factors including poor imaging, discontinuous structures, and rapidly varying salt-body geometries. All these factors may cause the above

Manuscript received by the Editor 25 July 2017; revised manuscript received 11 November 2017; published ahead of production 09 January 2018; published online 05 April 2018.

¹The University of Texas at Austin, Bureau of Economic Geology, Austin, Texas, USA. E-mail: xinming.wu@beg.utexas.edu; sergey.fomel@beg.utexas.edu; michael.hudec@beg.utexas.edu.

© 2018 Society of Exploration Geophysicists. All rights reserved.

attributes to fail to accurately detect the salt boundary and make salt boundary picking a highly challenging task.

In this paper, we present an efficient semiautomatic method to accurately extract 2D and 3D salt boundaries from seismic attribute images that highlight salt boundaries. We first adopt an optimal path picking algorithm (Fomel, 2009) to automatically extract a 2D salt boundary by picking the optimal path with globally maximum val-

ues within a salt boundary attribute image. The algorithm is robust to extract highly discontinuous salt boundaries, but it may fail to pick closed boundaries or highly dipping boundaries. We then propose a semiautomatic method to make this algorithm applicable to extract those closed and highly dipping salt boundaries. We further propose a way to extract a 3D salt boundary by first recursively picking 2D boundaries in the inline or crossline direction and then fitting these picked boundaries to obtain an implicit (level-set) surface of the 3D salt boundary. We finally discuss the application of our method in salt boundary picking with a combination of multiple types of seismic attributes.

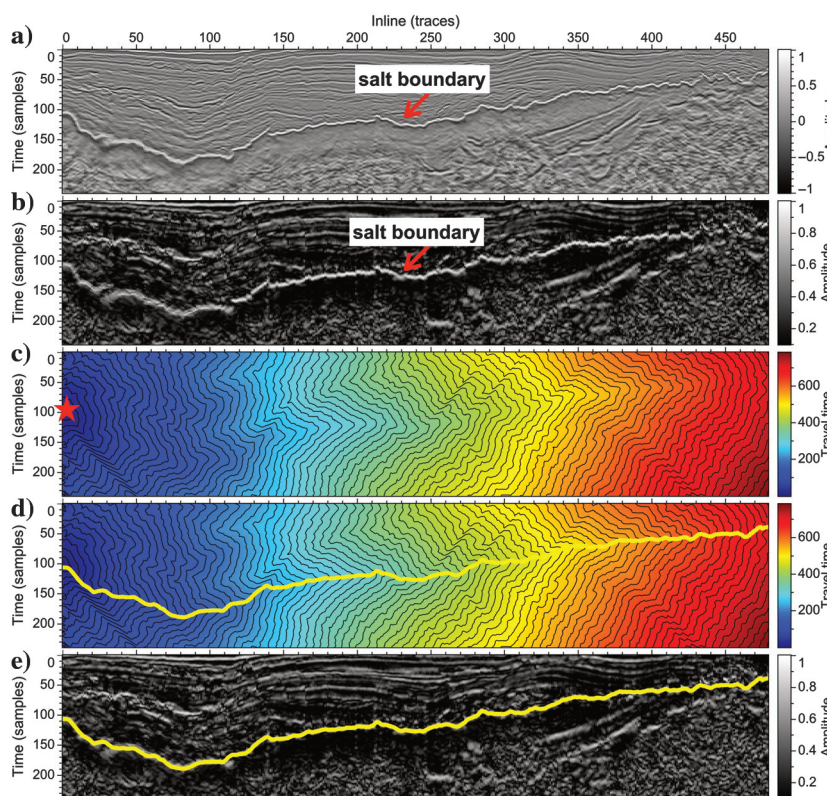


Figure 1. To pick a salt boundary with (a) relatively high amplitudes (b) the envelope image is used as a pseudovelocity map to compute a (c) traveltimemap, from which (d) the path with a globally minimal traveltimemap is picked. This picked path corresponds to the salt boundary with the globally highest amplitude values (e).

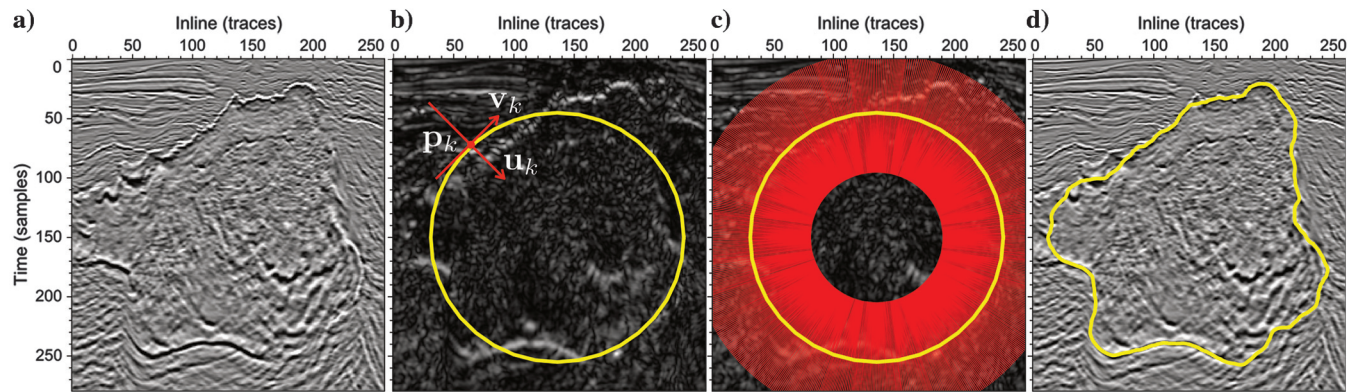


Figure 2. To pick the closed salt boundary in (a) the seismic amplitude image and (b) its corresponding envelope image, an initial circular curve (b) is first manually defined near the true salt boundary. The envelope image is then resampled within (c) a band area centered at the initial curve. This closed band area is then unwrapped to obtain a resampled image shown in Figure 3a. An optimal path (Figure 3b) with globally maximum envelope values is then picked from the resampled image and mapped back to obtain (d) a final salt boundary in the original seismic image.

OPTIMAL PATH PICKING

In a 2D seismic image (Figure 1a), a salt boundary can be typically recognized by strong reflections with relatively high amplitude values or by high values in another attribute. Therefore, we may consider salt boundary picking as a problem of searching for an optimal path with globally maximum values. As discussed by Fomel (2009), optimal path picking can be further considered as analogous to the ray tracing problem to find a minimum-traveltimemap trajectory that passes through globally maximum velocities.

In picking a salt boundary with high amplitude values, we first compute an envelope image $e(z, x)$ (Figure 1b) from the input seismic reflection image (Figure 1a) and we then try to find an optimal path $z(x)$ that maximizes the following integral over the path:

$$\int_{x_{\min}}^{x_{\max}} e(z(x), x) dx, \quad (1)$$

where x and z , respectively, represent the inline and depth coordinates of the input seismic image. To find such a path, we use the envelope image $e(z, x)$ as an input pseudovelocity map for the

ray-tracing problem to compute a trajectory with the minimum traveltime by solving the following eikonal equation (Fomel, 2009):

$$\left(\frac{\partial t}{\partial z}\right)^2 + \frac{1}{\lambda^2} \left(\frac{\partial t}{\partial x}\right)^2 = \exp[-2e(z, x)], \quad (2)$$

where λ is a scaling number and t is the traveltime to be computed. We solve this eikonal equation using a finite-difference algorithm and obtain a traveltime map shown in Figure 1c, where the black curves represent traveltime contours or wavefronts. We can observe that the fastest wavefronts follow the salt boundary with high amplitudes or pseudovelocities in Figure 1b. From the computed traveltime map (Figure 1c and 1d), the trajectory (the yellow curve in Figure 1d) with a minimum traveltime can be extracted by tracking backward along the traveltime gradient direction. This picked trajectory matches well with the salt boundary as shown in Figure 1e.

In computing the traveltime map in Figure 1c, we have assumed that the imaginary wave propagates from left to right and we placed the wave source (red star in Figure 1c) at the very left position: $x = 0$ and $z = 100$. Fortunately, the source location $z = 100$ in this case is close to the salt boundary depth at $x = 0$. In practice, we may not know the salt boundary position and the initial source location may get placed far away from the salt boundary. The picked fastest ray trajectory (from left to right) will then deviate from the true salt boundary at the beginning but will eventually follow the salt boundary at the end because the high pseudovelocities of the salt boundary will keep attracting the ray trajectory. Therefore, one way to correct the error due to an incorrect source position is to first propagate wave forward (from left to right) with the wrong source position to find the correct salt boundary position at the end and then use it as the new source position to propagate wave backward (from right to left) to find the fastest ray trajectory corresponding to the salt boundary.

In this first example (Figure 1), we have assumed that the salt boundary is relatively flat and extends from left to right, so that we can propagate the wave from left to right to find a ray trajectory corresponding to the salt boundary. This assumption, however, may not be true in most cases in which a salt boundary is a closed curve (2D) or a surface (3D) and the dip of the salt boundary can be significantly high and may vary rapidly. The ray tracing method described above may fail to pick a closed or highly dipping salt boundary. In the next section, we discuss a semiautomatic way to make this method applicable to extracting complicated 2D and 3D closed salt boundaries.

SALT BOUNDARY INTERPRETATION

Salt body interpretation often involves picking the top boundary, base boundary, and the closed boundary of the salt body from a migrated seismic image. The optimal path picking technique can be directly applied to pick relatively flat salt top and base boundaries such as the one in Figure 1. To pick a closed salt boundary or those top and base boundaries with high dips and rapid dip variations, we transform a seismic image into a new space in which the salt boundary is an open and relatively flat curve with slower dip variations.

2D salt boundary

To pick a closed salt boundary in Figure 2a, we first draw an initial boundary, which is a circle near the salt boundary as shown in Figure 2b. We can represent this initially specified curve \mathcal{P} as a set of N points that are evenly sampled on the curve in the clockwise order:

$$\mathcal{P} = \{\mathbf{p}_0, \mathbf{p}_1, \dots, \mathbf{p}_{N-1}\}, \quad (3)$$

where $\mathbf{p}_k = (x_k, y_k)$ for $k = 0, 1, \dots, N - 1$. With this initially specified curve, we resample the seismic image in a band area as denoted by the closely aligned red lines in Figure 2c. These red lines and the band area are centered at the initial curve (the yellow circle in Figure 2c). At each point \mathbf{p}_k on the curve, we sample the image in the \mathbf{u}_k direction (perpendicular to the initial yellow curve) and obtain a sequence of samples $\mathbf{s}_k(r)$ in a range $[-r_{\max}, r_{\max}]$, where r denote the distances between the samples and the centered point \mathbf{p}_k . The term r_{\max} should be large enough to include the true salt boundary in the sampling band area as denoted by red lines in Figure 2c. For all examples in this paper, we choose $r_{\max} = 50$, which can be smaller if the initially specified curve is closer to the true salt boundary.

By sampling in this way, we will obtain a set of sequences $\{\mathbf{s}_0(r), \mathbf{s}_1(r), \dots, \mathbf{s}_{N-1}(r)\}$, where each sequence $\mathbf{s}_k(r)$ contains a set of resampled image samples in directions parallel to the red lines or perpendicular to the initial yellow curve in Figure 2c. We then align this set of sequences horizontally to obtain a resampled image shown in Figure 3a, where the true salt boundary appears as an open curve with relatively high amplitude values. In this image (Figure 3a), the horizontal axis represents index (k) of points (\mathbf{p}_k) on the initially specified curve, whereas the vertical axis represents distances r away from the points (\mathbf{p}_k) in directions (\mathbf{u}_k) normal to the initial curve. From such a resampled image, we can use the previously discussed optimal picking algorithm to track the globally maximum (from left to right) path, which can be denoted by a sequence of distances $r_k(k \in 0, 1, \dots, N - 1)$. The yellow curve in Figure 3b shows the picked optimal path, which correctly follows the relatively high amplitudes.

From this picked path (a sequence of distances $r_k(k \in 0, 1, \dots, N - 1)$) picked in the resampled image, we are able to compute the true salt boundary (a set of points \mathbf{p}'_k) in the original image as follows:

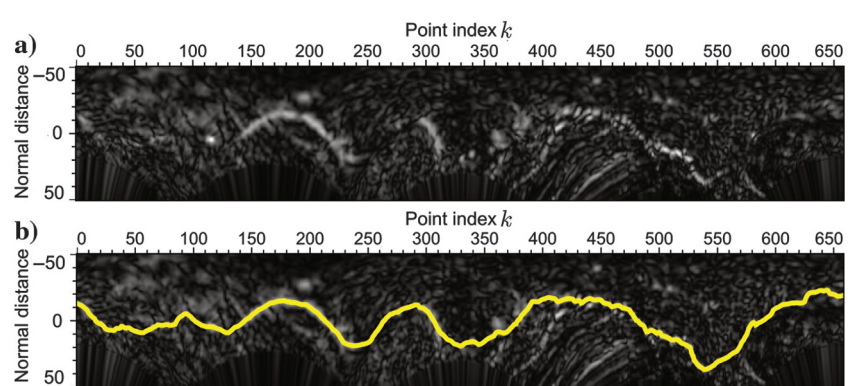


Figure 3. From (a) an resampled envelope image, an optimal path with globally maximum envelope values is picked as denoted by the yellow curve in (b).

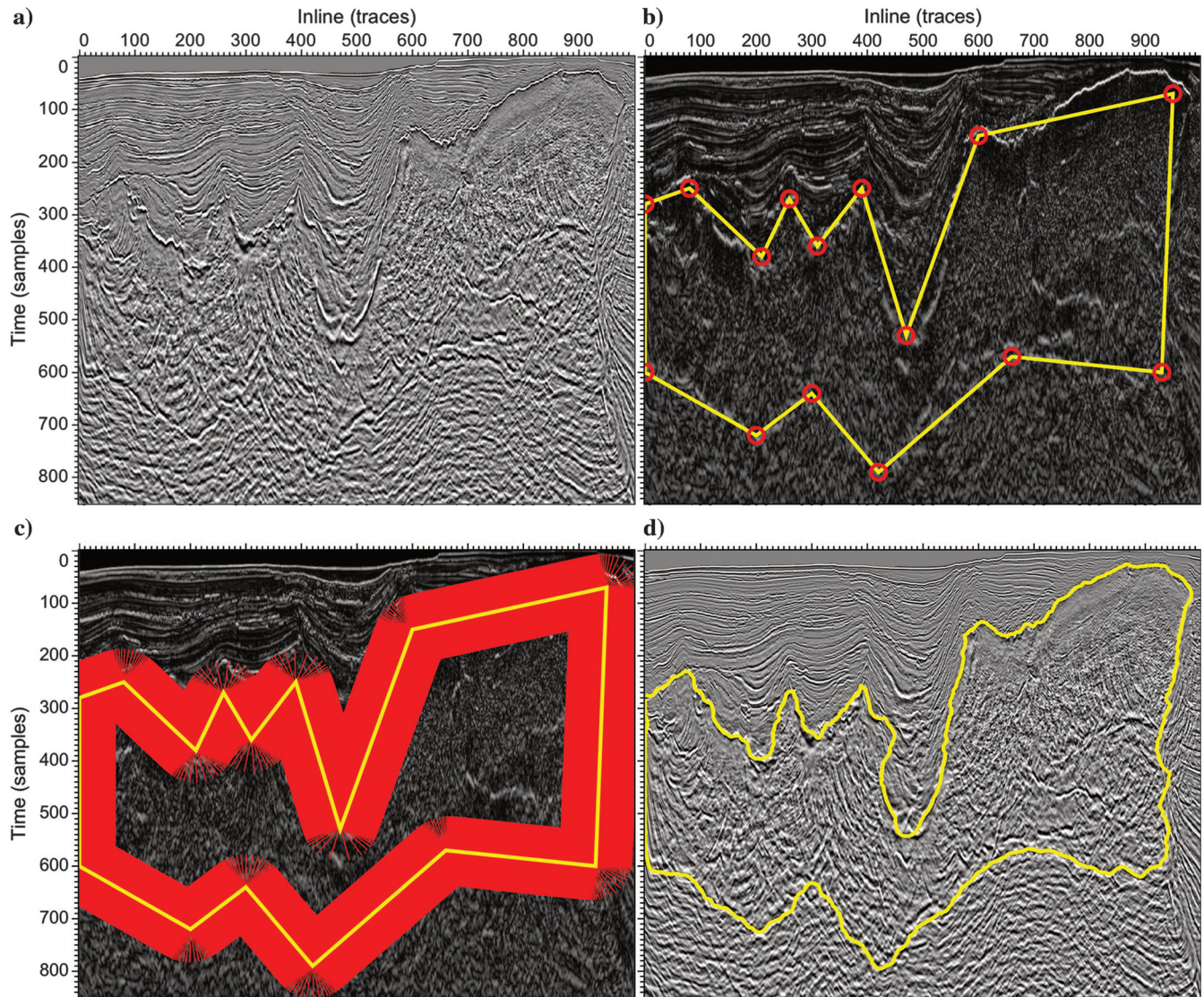


Figure 4. To pick the closed salt boundary in (a) the seismic amplitude image and (b) its corresponding envelope image, an initial enclosed curve (b) is first manually by picking several points (yellow circles) near the true salt boundary. (c) The envelope image is then resampled within a band area centered at the initial and obtain a corresponding resampled image shown in Figure 5a. An optimal path (Figure 5b) is then picked from the resampled image and mapped back to obtain a final salt boundary (d) in the original seismic image.

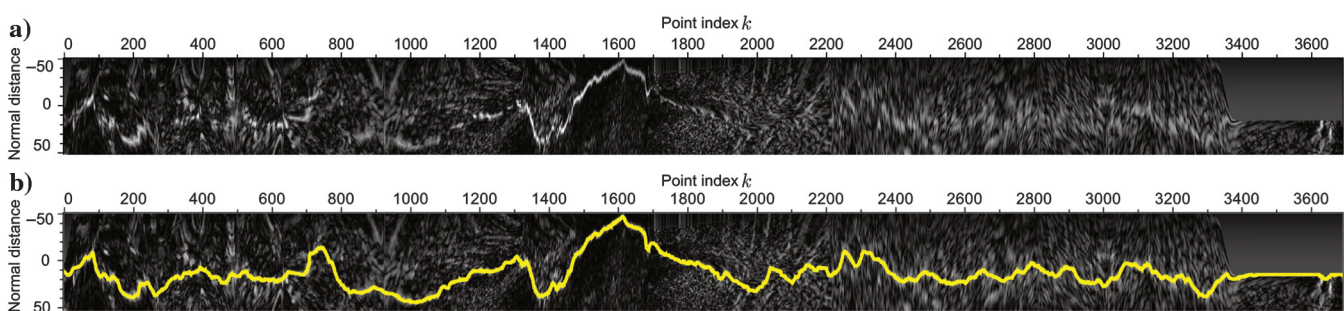


Figure 5. From (a) an resampled envelope image, an optimal path with globally maximum envelope values is picked as shown by the yellow curve in (b).

$$\mathbf{p}'_k = \mathbf{p}_k + r_k \mathbf{u}_k. \quad (4)$$

This equation means that our method updates the initial curve ($\mathcal{P} = \{\mathbf{p}_0, \mathbf{p}_1, \dots, \mathbf{p}_{N-1}\}$) to the final salt boundary ($\mathcal{P}' = \{\mathbf{p}'_0, \mathbf{p}'_1, \dots, \mathbf{p}'_{N-1}\}$) using only one step by shifting the initial curve in its normal directions (\mathbf{u}_k). The yellow curve in Figure 2d shows the salt boundary mapped from the picked optimal path in Figure 3b using equation 4.

In many cases, like the one in Figure 4a, the shape of a salt boundary can be much more complicated than the one shown in Figure 2. In these cases, we may need to define the initial curves with more complicated shapes, so that the true salt boundaries in the resampled images are relatively flat curves with slowly variant dips. To define such an initial curve, we first pick several control points (red circles in Figure 4b) and then we interpolate a curve (the yellow curve in Figure 4b) from these points using a simple linear interpolation method. To obtain an initial curve following the general structural trend of the true salt boundary, we suggest picking control points at corners or other singularities of the salt boundary. After defining an initial curve with control points in Figure 4b, we then follow the steps as in the previous example (Figure 2) to resample the seismic image in a band area (Figure 4c) centered at the initial curve and obtain a resampled image shown in Figure 5a. We then pick the global maximum path in this resampled image and finally map (equation 4) this picked path to the original image to obtain the salt boundary shown in Figure 4d. This final salt boundary correctly follows the true boundary, even in areas where the boundary is highly discontinuous.

Because the interpolated initial curve (Figure 4b) only needs to be close to the true salt boundary, the control points are not required to be picked exactly on the salt boundary, which makes the human interactions (picking the initial curve) convenient and efficient. However, these control points are allowed to be specified as hard control points in our algorithm if they are picked exactly on the true salt boundary. In this case, significantly high values (pseudovelocities) are manually defined at the control points to enforce the picked optimal path exactly passes through these control points. The hard control points can be helpful to incorporate human insights into the method in areas where the seismic salt boundary is highly unclear or the apparent seismic boundary does not follow the geology.

3D salt boundary

The 2D salt boundary picking method can be conveniently applied to interpret a 3D salt boundary by first recursively picking a sequence of 2D boundaries in the inline or crossline direction and then fitting these 2D boundaries to construct a 3D surface of the salt boundary. In picking the 2D salt boundaries in a sequence of inline or crossline slices, we do not need to manually

define an initial curve at every slice. In many cases, we only need to manually interpret an initial curve to pick a salt boundary at the first slice. We can then pick the salt boundary in the next slice by recursively using the previously picked salt boundary as an initial approximation. In most cases, such a previously picked salt boundary can be a better initial than a manually defined one (like those in Figures 2b and 4b) to follow the true boundary. In cases where a salt boundary varies rapidly from slice to slice, additional human interactions may be required to correct the initial curve picked from the previous slice.

Figure 6a shows a 3D seismic image with 550 inline slices, 850 crossline slices, and 850 depth samples. From this seismic amplitude image, we first compute an envelope as the input for the salt boundary picking. We also manually interpret nine initial curves, each for every 100 crossline slices, as denoted by the yellow curves in Figure 6b. With the input envelope image and the manually interpreted nine initial curves, we then compute the 2D salt bounda-

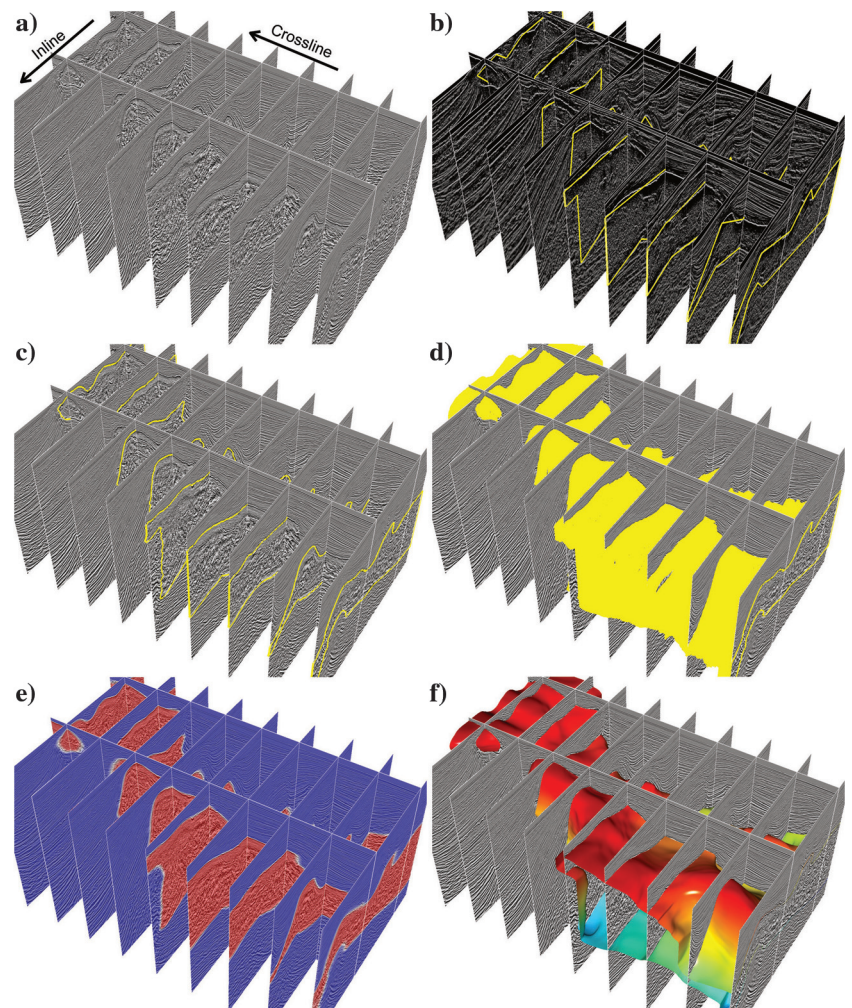


Figure 6. To pick the 3D salt boundary in (a) the seismic amplitude and (b) envelope images, nine initial curves (yellow curves in b)) are manually defined in nine inline slices. (c) These nine initial curves are first updated to the true salt boundaries, and then are used as (d) initial curves for the nearby slices to recursively pick 2D salt boundaries in all inline slices. (e) These picked 2D boundaries are used to fit an implicit function, from which (f) a 3D salt boundary is extracted as the zero contour surface colored by depth.

ries within the nine slices as denoted by yellow curves in Figure 6c. With these picked nine salt boundaries, we then recursively and automatically pick all the other 2D salt boundaries (the yellow curves in Figure 6d) in their nearby crossline slices.

With these 2D salt boundaries picked within all the crossline slices, our final step is to fit a 3D surface from these 2D curves. However, a 3D salt boundary can be a complicated and closed surface that may be difficult to define explicitly. We therefore define a 3D salt boundary as an implicit level-set function with positive values inside the salt boundary, zero values at the boundary, and negative values outside the boundary. From the sequence of picked 2D crossline salt boundaries, we can define such a 3D implicit function slice by slice in the crossline direction and we then apply Gaussian smoothing to obtain a smooth implicit function displayed with translucent colors overlaid with the seismic image in Figure 6e. In this image of the implicit function, blue colors outside the salt body represent negative values, red colors inside the salt body denote positive values, whereas the salt boundary is colored by white colors that represent zero values. From such an implicit function, a 3D salt boundary surface (colored by depth in Figure 6f) can be extracted by computing the zero contour of the implicit function. We efficiently compute such a zero contour using the classic marching cubes algorithm (Lorensen and Cline, 1987).

In this 3D example, we recursively pick 2D salt boundaries at all crossline slices and therefore directly obtain a 3D implicit function.

For the consideration of efficiency, in practice, we may recursively pick 2D salt boundaries on a coarser grid. Then we need to interpolate a 3D implicit function from these sparsely picked 2D boundaries or 2D implicit functions. Such a problem will be similar to the problem of surface reconstruction from sparse points, which is well studied in computer graphics. Numerous methods including the radial basis functions (Carr et al., 2001; Dinh et al., 2002) and Poisson's surface reconstruction (Kazhdan et al., 2006; Kazhdan and Hoppe, 2013; Wu, 2016) can be used to compute a 3D implicit function (such as the one in Figure 6e) from sparsely picked 2D salt boundaries.

SALT BOUNDARY PICKING WITH MULTIPLE ATTRIBUTES

In all the previous examples, we use a seismic envelope image as an input for salt boundary picking by assuming that a salt boundary reflection maintains its characteristic impedance across the area being picked. If something happens to change this impedance (for example, juxtaposition of salt against a piece of high-velocity rafted caprock), our methods may yield inaccurate results. In addition to the seismic envelope, other appropriate seismic attributes that highlight salt boundaries can also be used in the methods for salt boundary picking. More importantly, we may use a combination of multiple attributes if a salt boundary cannot be completely high-

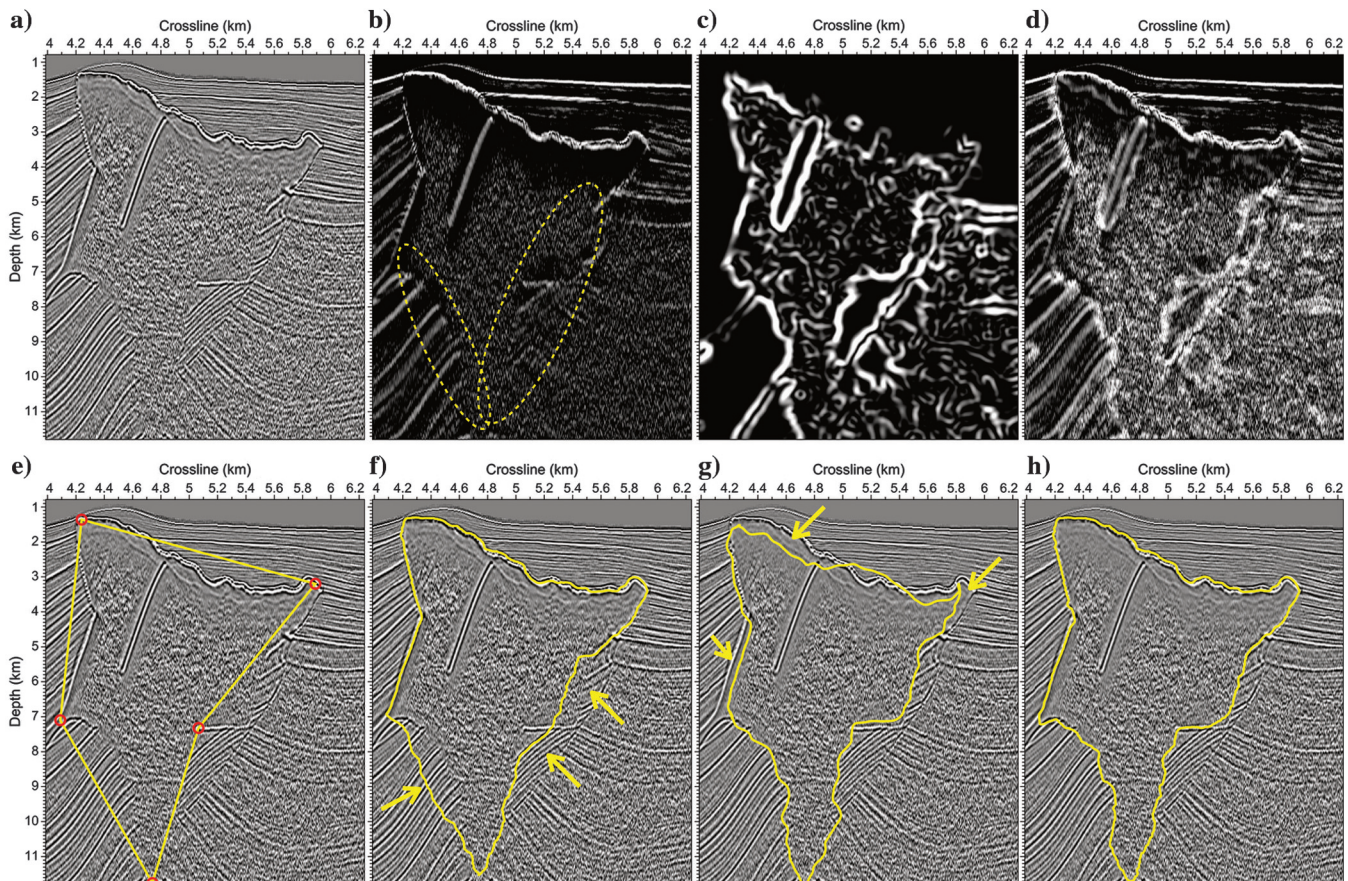


Figure 7. (a) Input 2D seismic image. (b) Envelope image. (c) Salt likelihood image. (d) Combined envelope and salt likelihood image. With (e) the same initial salt boundary interpolated from five control points, final salt boundaries (the yellow curves in [f-h]) are picked, respectively, from the envelope image, salt likelihood image, and combined envelope and salt likelihood image.

lighted by a single type of attributes. A simple way to incorporate multiple types of attributes into our method is to first compute an averaged summation of multiple attributes and then use it as an input pseudovelocity map for the salt boundary picking.

Figure 7 shows a 2D example that illustrates this simple way of using multiple attribute images. The 2D seismic amplitude image (Figure 7a) is extracted from the migrated depth image of the 3D SEG Advanced Modeling (SEAM) (Fehler and Keliher, 2011). In this 2D seismic image, the top part of the salt boundary is apparent as strong and continuous reflections, whereas the bottom part can be recognized as a boundary in which the linearity of image features significantly decreases from the outside to the inside of the salt body. The seismic envelope image (Figure 7b) highlights the top salt boundary with strong reflections but fails to detect the base of the salt boundary (denoted by ellipses in Figure 7b). The salt likelihood attribute (Wu, 2016) image (Figure 7c), computed as the gradient magnitude of reflection linearity or planarity (Hale, 2009; Wu, 2017), successfully highlights the base of the salt boundary but may fail to accurately detect the positions of the top salt boundary. We therefore sum the envelope and the salt likelihood images to obtain a combined attribute image (Figure 7d) where the top and the base of the salt boundary are apparent as relatively high amplitudes (white color).

In comparison of the salt boundary picking with the three different attribute images (Figure 7b–7d), we use the same initial curve (Figure 7e) interpolated from five manually interpreted points. Picking with the envelope image (Figure 7b), we obtain a final salt boundary (Figure 7f) which accurately follows the top of the true boundary but fails to follow the base in the areas denoted by yellow arrows in Figure 7f. However, using the salt likelihood image (Figure 7c), we obtain a picked final salt boundary (Figure 7g) that fits well with the base of the true boundary but fails to follow the top in the areas denoted by yellow arrows in Figure 7g. By using the combined attribute image (Figure 7d), we are able to obtain a finally picked curve that accurately follows the top and base of the true salt boundary.

Figure 8 shows a 3D example of salt boundary picking with a combination of multiple salt boundary attributes. The 3D seismic image (Figure 8a) is a subset ($550 \times 400 \times 450$ samples) of the migrated depth image of the SEAM (Fehler and Keliher, 2011). In picking the 3D salt boundary in this seismic image, we first compute a combined envelope and salt likelihood image as in the 2D example shown in Figure 7. The following steps are exactly the same as those in the 3D example shown in Figure 6. We then manually interpret nine initial curves (each one for every 50 inline slices) and use the combined salt attribute image to compute the final salt boundaries at the corresponding nine inline slices. With these picked nine salt boundaries, we further recursively and automatically pick all the other 2D salt boundaries in their nearby inline slices. With all these 2D salt boundaries picked within all inline slices, we finally compute an implicit function that is displayed with translucent colors overlaid with the seismic image in Figure 8b. In this implicit function, the salt body is represented by positive values and denoted by red colors in Figure 8b. From such an implicit function, the salt boundary is extracted as a zero-level-set surface which is colored by depth in Figure 8c.

The 3D salt boundary (Figure 8c) is fitted from recursively picked 2D inline salt boundaries. To check the consistency of the 2D inline salt boundaries in the crossline direction, we extract four

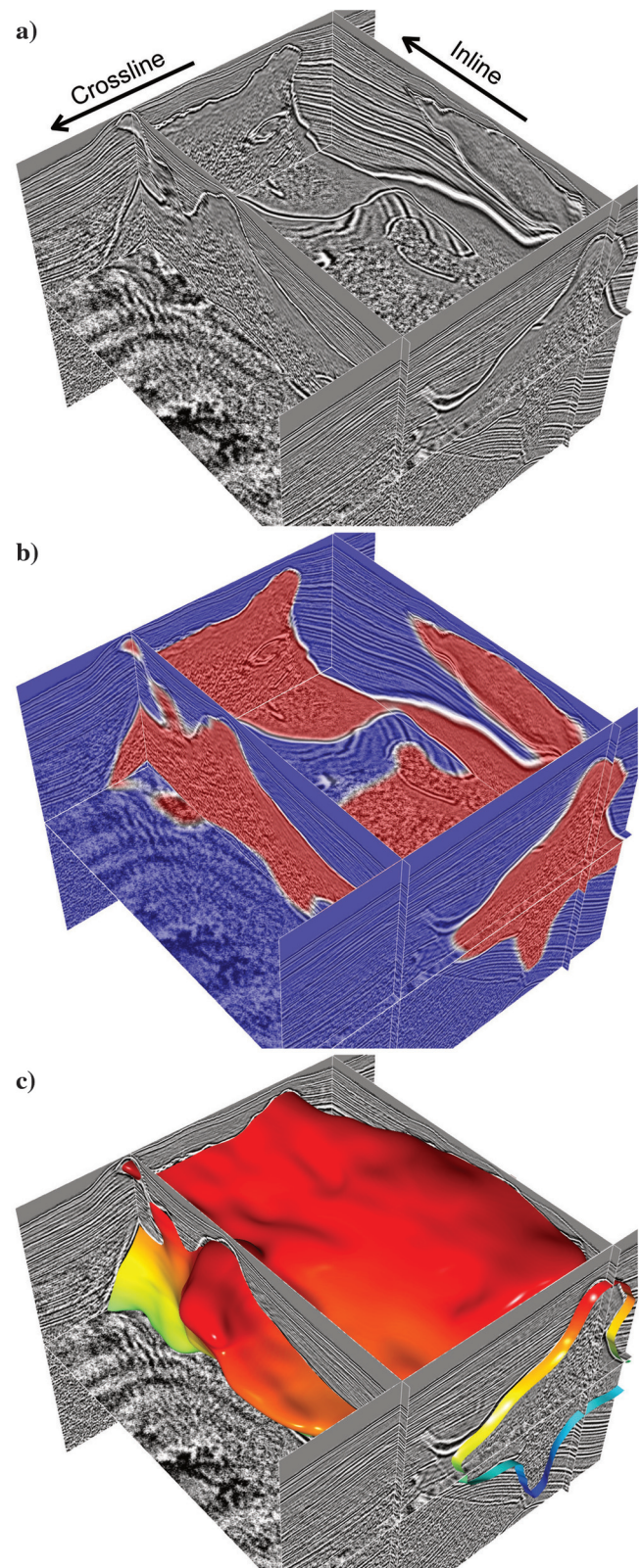


Figure 8. (a) Three-dimensional seismic amplitude image. (b) Implicit salt boundary function. (c) Three-dimensional salt boundary colored by depth.

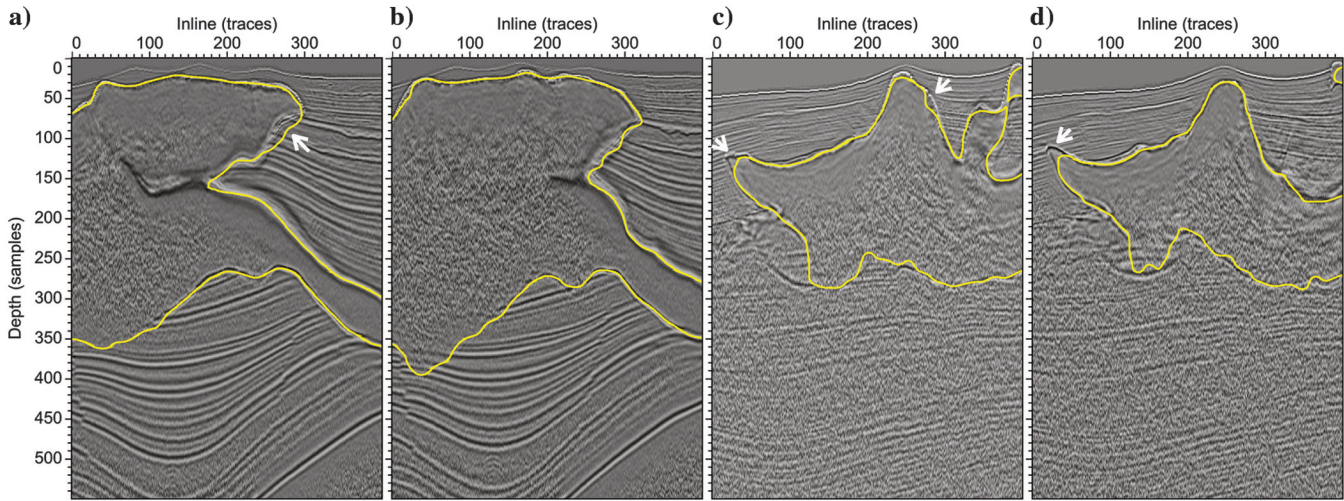


Figure 9. Four crossline slices with intersected salt boundaries are extracted from the 3D seismic image and the picked 3D salt boundary surface. The picked salt boundaries (yellow curves) are mostly correct but fail to correctly follow the true salt boundary at the positions highlighted by the white arrows.

crossline slices (Figure 9) with intersected salt boundaries (yellow curves) from the 3D seismic image and the fitted 3D salt boundary surface (Figure 8c). The intersected crossline salt boundaries are mostly correct but fail to correctly follow the true salt boundaries at the positions highlighted by white arrows. To further improve the result, we suggest to also recursively pick 2D salt boundaries in the crossline direction and then fit a 3D salt boundary surface with the inline and crossline salt boundaries.

CONCLUSION

We have proposed a semiautomatic method to efficiently pick 2D and 3D salt boundaries that may be complicated by noise, discontinuous structures, and rapidly space-variant folding. While picking a complicated 2D salt boundary, we first compute a salt boundary attribute (envelope) image and initiate a curve close to the boundary by picking a limited number of points near the boundary. With this initial curve, we then resample the attribute image in a band area centered at the initial curve and obtain a new image, where the salt boundary is an open curve with relatively flat and slowly varying dips. We further pick the optimal path with globally maximum values within the resampled image. We finally map the picked optimal path back to the original seismic image to obtain a final salt boundary.

While picking a 3D complicated salt boundary, we directly apply the 2D boundary picking method to recursively pick a sequence of 2D boundaries in the inline or crossline directions. We then fit these picked 2D boundaries to construct a 3D implicit (level-set) surface of the salt boundary. In this recursive picking, human interactions are greatly reduced using the salt boundary picked in the previous slice as an initial for picking the salt boundary in a followed slice. For all examples in this paper, we recursively pick only the inline salt boundaries and we then fit an implicit surface of a 3D salt boundary. In practice, we can recursively pick the inline and crossline boundaries to fit a better 3D salt boundary. The computational time of the salt boundary picking is mainly spent on the optimal path picking, and our implementation takes approximately 1 min on an eight-core laptop to pick the 3D salt boundary in Figure 6.

ACKNOWLEDGMENTS

This research is financially supported by the sponsors of the Texas Consortium for Computation Seismology (TCCS). The 2D and 3D real seismic images are generously provided by CGG. The SEAM image in Figures 7 and 8 is provided through the SEG website (<http://seg.org/News-Resources/Research-Data/Open-Data>).

REFERENCES

- Amin, A., and M. Deriche, 2015, A hybrid approach for salt dome detection in 2D and 3D seismic data: 2015 IEEE International Conference on Image Processing (ICIP), 2537–2541.
- Aqrawi, A. A., T. H. Boe, and S. Barros, 2011, Detecting salt domes using a dip guided 3D sobel seismic attribute: 81st Annual International Meeting, SEG, Expanded Abstracts, 1014–1018.
- Asjad, A., and D. Mohamed, 2015, A new approach for salt dome detection using a 3D multidirectional edge detector: Applied Geophysics, **12**, 334–342, doi: [10.1007/s11770-015-0512-2](https://doi.org/10.1007/s11770-015-0512-2).
- Berthelot, A., A. H. Solberg, and L.-J. Gelius, 2013, Texture attributes for detection of salt: Journal of Applied Geophysics, **88**, 52–69, doi: [10.1016/j.jappgeo.2012.09.006](https://doi.org/10.1016/j.jappgeo.2012.09.006).
- Carr, J. C., R. K. Beatson, J. B. Cherrie, T. J. Mitchell, W. R. Fright, B. C. McCallum, and T. R. Evans, 2001, Reconstruction and representation of 3d objects with radial basis functions: Proceedings of the 28th Annual Conference on Computer Graphics and Interactive Techniques, ACM, 67–76.
- Dahlke, T., R. Clapp, and B. Biondi, 2016, Second-order updating in shape optimization for salt segmentation, 86th Annual International Meeting, SEG, Expanded Abstracts, 5369–5373.
- Di, H., and G. AlRegib, 2017, Seismic multi-attribute classification for salt boundary detection: A comparison: 79th Annual International Conference and Exhibition, EAGE, Extended Abstracts, doi: [10.3997/2214-4609.201700919](https://doi.org/10.3997/2214-4609.201700919).
- Di, H., M. A. Shafiq, and G. AlRegib, 2017, Multi-attribute k-means cluster analysis for salt boundary detection: 79th Annual International Conference and Exhibition, EAGE, Extended Abstracts, doi: [10.3997/2214-4609.201700915](https://doi.org/10.3997/2214-4609.201700915).
- Dinh, H. Q., G. Turk, and G. Slabaugh, 2002, Reconstructing surfaces by volumetric regularization using radial basis functions: IEEE Transactions on Pattern Analysis and Machine Intelligence, **24**, 1358–1371, doi: [10.1109/TPAMI.2002.1039207](https://doi.org/10.1109/TPAMI.2002.1039207).
- Fehler, M., and P. Kelher, 2011, Seam phase 1: Challenges of subsalt imaging in tertiary basins, with emphasis on deepwater gulf of mexico: SEG.
- Fomel, S., 2009, Velocity analysis using AB semblance: Geophysical Prospecting, **57**, 311–321, doi: [10.1111/j.1365-2478.2008.00741.x](https://doi.org/10.1111/j.1365-2478.2008.00741.x).
- Hale, D., 2009, Structure-oriented smoothing and semblance: CWP Report, Colorado School of Mines.
- Halpert, A., and R. G. Clapp, 2008, Salt body segmentation with dip and frequency attributes: SEP.

- Halpert, A. D., R. G. Clapp, and B. Biondi, 2014, Salt delineation via interpreter-guided 3D seismic image segmentation: *Interpretation*, **2**, no. 2, T79–T88, doi: [10.1190/INT-2013-0159.1](https://doi.org/10.1190/INT-2013-0159.1).
- Haukås, J., O. R. Ravndal, B. H. Fotland, A. Bounaim, and L. Sonneland, 2013, Automated salt body extraction from seismic data using the level set method: *First Break*, **31**, no. 4, 35–42, doi: [10.3997/1365-2397.2013009](https://doi.org/10.3997/1365-2397.2013009).
- Hegazy, T., and G. AlRegib, 2014, Texture attributes for detecting salt bodies in seismic data: 84th Annual International Meeting, SEG, Expanded Abstracts, 1455–1459.
- Hudec, M. R., M. P. Jackson, B. C. Vendeville, D. D. Schultz-Ela, and T. P. Dooley, 2011, The salt mine: A digital atlas of salt tectonics: Bureau of Economic Geology, Jackson School of Geosciences, University of Texas at Austin.
- Jackson, M. P., and M. R. Hudec, 2016, Salt tectonics: Principles and practice: Cambridge University Press.
- Jing, Z., Z. Yanqing, C. Zhigang, and L. Jianhua, 2007, Detecting boundary of salt dome in seismic data with edge-detection technique: 77th Annual International Meeting, SEG, Expanded Abstracts, 1392–1396.
- Kazhdan, M., M. Bolitho, and H. Hoppe, 2006, Poisson surface reconstruction: Proceedings of the fourth Eurographics Symposium on Geometry Processing, 61–70.
- Kazhdan, M., and H. Hoppe, 2013, Screened Poisson surface reconstruction: *ACM Transactions on Graphics (TOG)*, **32**, 1–13, doi: [10.1145/2487228](https://doi.org/10.1145/2487228).
- Leveille, J. P., I. F. Jones, Z.-Z. Zhou, B. Wang, and F. Liu, 2011, Subsalt imaging for exploration, production, and development: A review: *Geophysics*, **76**, no. 5, WB3–WB20, doi: [10.1190/geo2011-0156.1](https://doi.org/10.1190/geo2011-0156.1).
- Lomask, J., R. G. Clapp, and B. Biondi, 2007, Application of image segmentation to tracking 3D salt boundaries: *Geophysics*, **72**, no. 4, P47–P56, doi: [10.1190/1.2732553](https://doi.org/10.1190/1.2732553).
- Lorensen, W. E., and H. E. Cline, 1987, Marching cubes: A high resolution 3D surface construction algorithm: *ACM Siggraph Computer Graphics*, *ACM*, **21**, 163–169, doi: [10.1145/37402](https://doi.org/10.1145/37402).
- Ramirez, C., G. Larrazabal, and G. Gonzalez, 2016, Salt body detection from seismic data via sparse representation: *Geophysical Prospecting*, **64**, 335–347, doi: [10.1111/1365-2478.12261](https://doi.org/10.1111/1365-2478.12261).
- Wang, B., Y. Kim, C. Mason, and X. Zeng, 2008, Advances in velocity model-building technology for subsalt imaging: *Geophysics*, **73**, no. 5, VE173–VE181, doi: [10.1190/1.2966096](https://doi.org/10.1190/1.2966096).
- Wang, Z., T. Hegazy, Z. Long, and G. AlRegib, 2015, Noise-robust detection and tracking of salt domes in postmigrated volumes using texture, tensors, and subspace learning: *Geophysics*, **80**, no. 6, WD101–WD116, doi: [10.1190/geo2015-0116.1](https://doi.org/10.1190/geo2015-0116.1).
- Wu, X., 2016, Methods to compute salt likelihoods and extract salt boundaries from 3D seismic images: *Geophysics*, **81**, no. 6, IM119–IM126, doi: [10.1190/geo2016-0250.1](https://doi.org/10.1190/geo2016-0250.1).
- Wu, X., 2017, Directional structure-tensor based coherence to detect seismic faults and channels: *Geophysics*, **82**, no. 2, A13–A17, doi: [10.1190/geo2016-0473.1](https://doi.org/10.1190/geo2016-0473.1).
- Zhang, Y., and A. D. Halpert, 2012, Enhanced interpreter-aided salt boundary extraction using shape deformation: 82nd Annual International Meeting, SEG, Expanded Abstracts, doi: [10.1190/segam2012-1337.1](https://doi.org/10.1190/segam2012-1337.1).